

Topology and Shape Optimization of Ultrathin Composite Self-Deployable Shell Structures with Cutouts

Serena Ferraro * and Sergio Pellegrino †

California Institute of Technology, Pasadena, CA, 91125, United States

March 6, 2021

The paper presents two methods to design cutouts that allow damage-free folding of the stiffest possible composite self-deployable thin shell structures of complex shapes. The first method uses level-set functions that define a general number of cutouts. The second method uses a spline representation of the contour of a single cutout and optimizes its shape. Material failure detection is implemented in the solution. Both methods are applied to the design of deployable thin shells forming 90° joints, and multiple viable solutions are obtained. Experiments on the best performing design, a 90-390 μm thick shell made of Astroquartz with a cyanate ester matrix, with 5 cutouts on each side, are presented to illustrate and validate the proposed approach.

Nomenclature

F_x, F_y	=	In-plane failure strengths, combination of failure coefficients
$F_{1t} = F_{2t}$	=	Tensile strength parameters
$F_{1c} = F_{2c}$	=	Compressive strength parameters
F_3, F_4, F_6	=	In-plane shear, bending, and twisting strength parameters
FI_1	=	In-plane failure index
FI_2	=	Bending failure index
FI_3	=	Coupled in-plane and bending failure index

*Currently at: NASA Jet Propulsion Laboratory, 4800 Oak Grove Drive, Pasadena, CA 91109. email: serena.ferraro@jpl.nasa.gov .

†Joyce and Kent Kresa Professor of Aerospace and Civil Engineering, Graduate Aerospace Laboratories, 1200 East California Boulevard, Mail Code 105-05. AIAA Fellow. email: sergiop@caltech.edu.

Presented at SciTech 2019, January 7-11, 2019, San Diego as paper AIAA-2019-1524.

f_i, f_{ij}	=	Failure coefficients, combination of strength parameters
K_B	=	Deployed bending stiffness of shell
M_x, M_y, M_{xy}	=	Bending and twisting moment resultants for a flat plate
N_x, N_y, N_{xy}	=	In-plane and shear stress resultants for a flat plate
$RP_{center}, RP_{left}, RP_{right}$	=	Reference points for boundary conditions
U_x, U_y, U_z	=	Displacements in Cartesian coordinate system
ΔM_0	=	Initial bending moment
$\Delta \theta_0$	=	Initial folding angle
$\theta_{x-RP_{center}}, \theta_{x-RP_{left}}, \theta_{x-RP_{right}}$	=	Folding angles in Cartesian coordinate system

I. Introduction

ULTRATHIN COMPOSITE SHELL STRUCTURES, where a shell is defined as ultrathin if the wall thickness is smaller than $400 \mu\text{m}$, provide a versatile low-cost solution for many kinds of deployable structures. The introduction of small cutouts enables damage-free elastic folding that, combined with reverse snap-through that provides self-locking into the deployed configuration, can result in stiff, lightweight, and remarkably simple-looking structures. However, only a relatively narrow range of structural configurations have been considered so far, mostly straight booms with parallel dogbone cutouts [1, 2], and engineering intuition has played a significant role in the identification of suitable configurations for the cutouts. The general aim of this paper is applying this folding technique to more general situations.

The paper considers the problem of folding a shell with a complex geometry by introducing cutouts, and deploys different tools from the literature on structural optimization of thin shells to demonstrate and experimentally validate the automatic design of cutouts. Both single and multiple cutouts are included in the design space that is investigated, and it is found that the best performing solutions include both types.

Previous studies have optimized the length of cutouts in the edge stiffeners of deployable reflectors [3] as well as the length, width, and end hole diameter of slots in composite tape-spring hinges [4]. There is a rich literature on structural topology optimization, which includes widely used density-based methods, first formalized by Bendsøe and Kikuchi [5], and level-set methods, introduced by Osher and Sethian [6]. A comprehensive review of these methods was presented by Sigmund and Maute [7]. A study by Ye et al. [8] used a level-set method that allows the formation of cutouts to optimize shell structures, but without including geometric or material nonlinearities. Level-set topology optimization methods were also used by Maute et al. [9] to optimize 3D printed composites, and by Geiss et al. [10], for shell structures undergoing large deformations. This existing literature is very relevant to the problem to hand, but it should also be noted that the minimization of structural compliance by optimizing the voids (cutouts) and subject to stress constraints in the folded configuration of a deployable structure poses several unique challenges. The approach

chosen in the present paper is a level-set method, in order to allow consideration of a wide range of cutout designs while also keeping the computational effort manageable. An implementation of a density-based method for the cutout optimization of deployable booms can be found in [11].

A specific structure consisting of two cylinders forming a 90° corner joint, as shown in Fig. 1, is studied in this paper. The diameter of each cylinder is 32 mm and the distance from the end of a cylinder to the inner intersection is 200 mm. The structure is made of plain-weave 525 Astroquartz[®] II fabric (quartz fiber) [12], pre-impregnated with PMT-F6 cyanate ester resin [13], and the thickness ranges between 90 and $390\ \mu\text{m}$. The most highly deformed region, at the intersection between the two cylinders and shown in red in Fig. 1, consists of a two-ply laminate $[45_{pw}]_2$, where the 0° direction corresponds to the axis of each cylinder. The thinnest laminate was used in this region to minimize bending related effects. Thicker laminates with up to six plies were used in the rest of the structure.

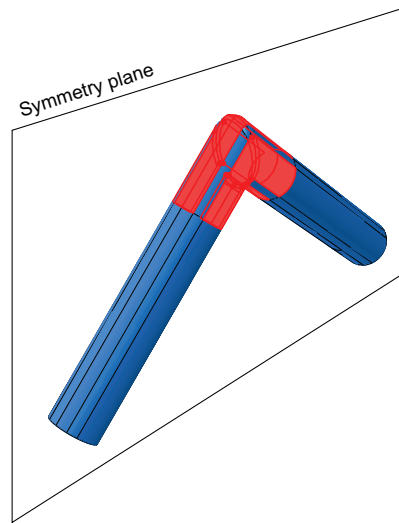


Fig. 1 Thin shell self-deployable joint with two-ply region shown in red.

The aim of the study is to transform this structure into a deployable joint that can be folded without damage. A folding angle of 45° was chosen, to shorten the time required to carry out geometrically nonlinear finite element simulations and hence to allow fast numerical simulations for the optimization studies. Nonconvergence of iterative finite element solvers is an issue when implementing large displacement simulations of deployable thin shells. Previous authors have addressed this issue by running explicit simulations with very small increments to obtain accurate results [2, 14–16] and benchmark problems that compare the implicit and explicit solvers of the Sierra Solid Mechanics code have been proposed [17, 18]. Generally, the drawback of choosing an explicit solver is longer simulation times, not a viable option for optimization studies, and therefore an implicit solver was adopted for the present study. The chosen folding angle allowed the study to capture the geometrically nonlinear effects associated with the folding of a corner joint, but avoided the effects of self-contact that would develop for larger folding angles. These effects are also of practical interest for the design of deployable shell structures and will be a topic of future research.

The specific objective of the study is to identify designs for the cutouts in this structure that allow it to withstand folding through 45° without any damage. The compliance of the resulting structures in the fully deployed configuration is to be minimized.

It should be noted that the shell has a vertical plane of mirror symmetry, shown in Fig. 1, and all of the cutouts considered in this study maintain this symmetry. Therefore, only the cutouts on one side of the shell will be explicitly discussed and a second set on the other side is assumed.

Two analytical tools were used to carry out this work. First, a finite element software was used to compute the stiffness of each candidate structural design in the deployed configuration and to carry out folding simulations for each design, in order to determine the stress distribution in the folded configuration. Second, a material failure criterion for the two-ply quartz laminate was implemented. These tools are presented in Section II. Section III presents designs based either on the simple approach of placing cutouts in the regions of the shell with the highest values of the failure indices in the folded configuration, or to use cutouts inspired by previous deployable boom designs, without any formal optimization. Section IV introduces the problem of optimizing the number, location, and shape of cutouts in a shell to allow folding without damage while maximizing the deployed stiffness. Section IV.A presents an optimization approach that uses level-set functions. The best performing design obtained from this approach was implemented, built and tested. Section IV.B presents the shape optimization of a single cutout. Section V summarizes the outcomes of the study and compares the designs obtained. Section VI concludes the paper.

II. Analytical Methods

Finite element simulations were used to analyze the deformation of trial designs of the deployable joint. A failure criterion for two-ply plain-weave laminates was implemented to numerically detect the onset of failure in the most highly stressed region of the joint.

Each simulation computed the bending stiffness of the joint in the initial configuration and the values of the failure indices at each step of the folding process.

A. Finite Element Simulations and Model Parameters

Geometrically nonlinear finite element simulations were carried out with the commercial software Abaqus 2017. After testing different types of shell elements (S3, S4, and S4R), the S4R elements were chosen because these reduced integration elements run faster and provide results in agreement with experimental results.

The composite layup was not defined explicitly. Instead, the laminate stiffness matrix was defined using the feature "general section properties" in Abaqus, which allows to manually input the **ABD** stiffness matrix of a shell.

Following Soykasap [19] the **ABD** matrix of the laminates was calculated with the mosaic model and the correction factor α (defined as the ratio between the values of D_{11} from the mosaic model and the measured values) was applied

to all terms of the D matrix to account for the mosaic model's over-prediction of the bending and twisting stiffnesses for laminates with small numbers of plies. The value of α for each laminate was measured from 4-point bending experiments [11] and is presented in Table 1. The effect of the crimp angle on the A matrix is relatively small and was neglected [19]. As expected from [19], the values of α decrease and tend to 1 as the number of plies increases.

Laminate	Average $D_{11_{\text{expt}}}$	Samples	Standard Deviation	α
$[45_{pw}]_2$	3.1	3	0.26	2.34
$[45_{pw}/0_{pw}/45_{pw}]$	10.0	5	0.34	2.19
$[45_{pw}]_4$	23.0	5	1.10	1.69
$[45_{pw}/45_{pw}/0_{pw}]_s$	69.8	5	1.30	1.30

Table 1 Bending stiffness D_{11} (Nmm) and reduction factor α for two- to six-ply laminates.

The A matrix for the laminate at the center of the deployable joint, $[45_{pw}]_2$, was

$$A_{[45_{pw}]_2} = \begin{bmatrix} 3403.2 & 1872.0 & 0 \\ 1872.0 & 3403.2 & 0 \\ 0 & 0 & 2150.3 \end{bmatrix} \text{ (N/mm)} \quad (1)$$

and the D matrix, after introducing the correction factor α , was

$$D_{[45_{pw}]_2} = \begin{bmatrix} 3.10 & 1.71 & 0 \\ 1.71 & 3.10 & 0 \\ 0 & 0 & 1.96 \end{bmatrix} \text{ (Nmm)} \quad (2)$$

The B matrix was zero because the laminate is symmetric.

The boundary conditions applied to the finite element model are shown in Fig. 2. Three massless reference points, $RP1$, $RP2$, and $RP3$, were defined. Two rectangular patches, shown in red, were coupled to the left and right reference points such that the in-plane rotations of the patches, θ_x , match the rotations imposed to the reference points. The sum of the rotations of the left and right reference points was set equal to the rotation of the center one, and was increased from 0° to 45° . With this boundary condition the end reaction moments are set equal. Finally, two nodes at the bottom of the shell, shown by red dots in Fig. 2, were constrained to remain in the y - z plane and the three translations of the node at the top of the shell were all set to zero.

The simulations were carried out with the Abaqus implicit solver that uses Newton-Raphson iterations to enforce equilibrium between the internal forces and the external loads. Convergence settings based on "half-increment residual

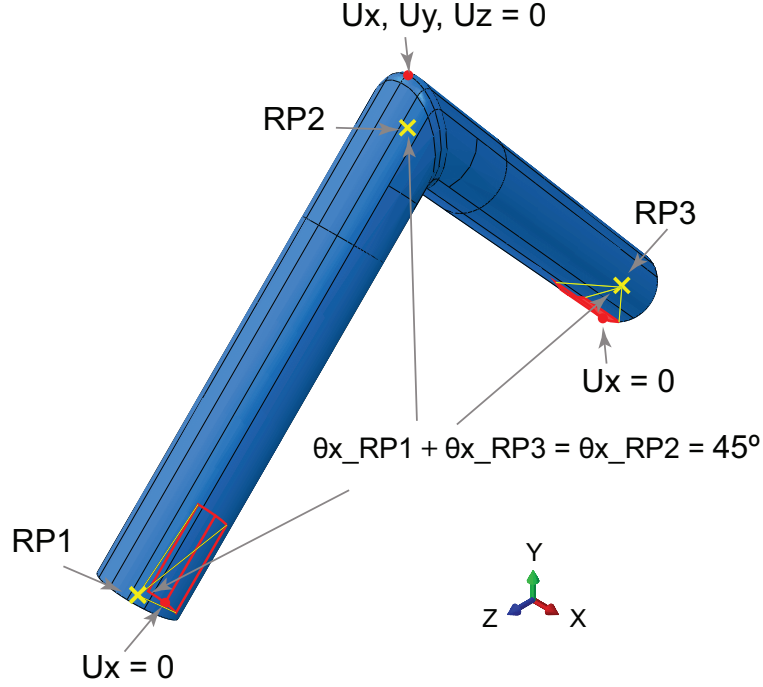


Fig. 2 Finite element model and boundary conditions.

tolerance" were used. This tolerance represents the equilibrium residual error (out-of-balance forces) halfway through a time increment. If the half-increment residual is small, it indicates that the accuracy of the solution is high and that the time step can be increased; conversely, if the half-increment residual is large, the time step used in the solution should be reduced. The Abaqus default half-increment residual tolerance, which is set at 10^{-3} times the time average force and moment values, was used.

B. Failure Criterion

Failure predictions during folding were made using the laminate failure criterion by Mallikarachchi and Pellegrino [20]. This criterion, developed for two-ply plain-weave carbon fiber composites, is applicable to laminates with fibers of any material and with an even number of plain-weave plies. Hence, it can be applied to the laminate at the center of the deployable joint.

The criterion uses three non-dimensional failure indices to capture in-plane, bending, and coupled in-plane and bending failures, defined as follows

$$FI_1 = f_1(N_x + N_y) + f_{11}(N_x^2 + N_y^2) + f_{12}N_xN_y + f_{33}N_{xy}^2 < 1 \quad (3)$$

$$FI_2 = f_{44} \times \max(M_x^2, M_y^2) + f_{66}M_{xy}^2 < 1 \quad (4)$$

$$FI_3 = \max\left(\frac{N_x}{F_x}, \frac{N_y}{F_y}\right) + \frac{\max(|M_x|, |M_y|)}{F_4} < 1 \quad (5)$$

where the failure coefficients, f_i and f_{ij} , are given by

$$f_1 = f_2 = \frac{1}{F_{1t}} - \frac{1}{F_{1c}} \quad (6a)$$

$$f_{11} = f_{22} = \frac{1}{F_{1t}F_{1c}} \quad (6b)$$

$$f_{12} = -\frac{f_{11}}{2} \quad (6c)$$

$$f_{33} = \frac{1}{F_3^2} \quad (6d)$$

$$f_{44} = f_{55} = \frac{1}{F_4^2} \quad (6e)$$

$$f_{66} = \frac{1}{F_6^2} \quad (6f)$$

and

$$F_x = \frac{-(f_1 + f_{12}N_y) \pm \sqrt{(f_1 + f_{12}N_y)^2 - 4f_{11}(f_1N_y + f_{11}N_y^2 + f_{33}N_{xy}^2 - 1)}}{2f_{11}} \quad (7a)$$

$$F_y = \frac{-(f_1 + f_{12}N_x) \pm \sqrt{(f_1 + f_{12}N_x)^2 - 4f_{11}(f_1N_x + f_{11}N_x^2 + f_{33}N_{xy}^2 - 1)}}{2f_{11}} \quad (7b)$$

The terms F_i represent directly measured or calculated strengths in the tow directions, and the subscripts t and c denote tension and compression, respectively. In a plain-weave laminate $F_{1t} = F_{2t}$ and $F_{1c} = F_{2c}$.

The tensile strength was measured as the smallest failure stress resultant obtained from tensile tests on plain-weave $[0_{pw}]_2$ laminates on 15 mm wide test samples. The compressive strength was calculated using elasto-plastic fiber microbuckling theory [21]

$$F_{1c} = \frac{G}{1 + \frac{\phi_0}{\gamma_y}} t \quad (8)$$

where ϕ_0 is the fiber misalignment angle, measured from micrographs of the laminate, γ_y is the in-plane yield shear strain, and t is the tow thickness. γ_y was derived from direct measurements of the shear strength τ_y , with

$$\gamma_y = \frac{\tau_y}{G} \quad (9)$$

and G is the shear modulus of a composite tow

$$G = \frac{G_m(G_{12f} + G_m + V_f(G_{12f} - G_m))}{G_{12f} + G_m - V_f(G_{12f} - G_m)} \quad (10)$$

The reason why the compressive strength was not obtained from direct measurements is that it has been shown [22] that compression tests on thin plain-weave composites have a low success rate due to test sample delamination and other spurious failure modes occurring instead of fiber microbuckling. It was found [22] that the prediction method described above estimates the microbuckling failure load with good accuracy. The in-plane shear strength, F_3 , was measured from tension tests on $[45_{pw}]_2$ laminates. The bending strength, F_4 , and the twisting strength, F_6 , were obtained from the smallest failure moments measured from platen bending tests [20, 23, 24] respectively on $[0_{pw}]_2$ and $[45_{pw}]_2$ laminates.

Table 2 shows the resulting strength parameters for two-ply laminates.

Strength Parameter	Average Value	Samples Tested	Standard Deviation
$F_{1t} = F_{2t}$ [N/m]	76.16	5	2.83
$F_{1c} = F_{2c}$ [N/mm]	34.50	-	-
F_3 [N/mm]	14.55	5	0.12
F_4 [N]	3.26	4	0.28
F_6 [N]	1.10	4	0.06

Table 2 Material strength parameters for two-ply laminates of Astroquartz[®] fiber and cyanate ester resin.

Initially, the three failure indices in Eqs. 3-5 were calculated at each step of the folding simulations and it was found that FI_1 was the largest of the three and the only failure index with values above 1. Because of the extreme thinness of the shells, FI_2 and FI_3 tend to be smaller. Therefore, it was decided to focus on FI_1 in the optimization study.

III. Preliminary Designs

Folding simulations of the shell without any cutouts were used to identify an initial location for a set of two identical cutouts, symmetrically placed on each side of the joint. Figure 3 shows the mid-plane stress resultants in the longitudinal direction of the two cylinders. The figure shows two peaks, one tensile and one compressive, in a narrow region at the center of the shell.

Based on this initial result, it was conjectured that the cutout topology problem could be solved simply by “drilling out” the most highly stressed part of the shell. Hence, a series of joints with circular cutouts over the stress peak region in Fig. 3 were analyzed. These attempts were all unsuccessful, even when the cutout with an initial diameter of 14 mm was enlarged.

An example is shown in Fig. 4, which shows a plot of FI_1 in the two-ply region of the joint. White areas of the plot are regions corresponding to cutouts or parts of the shell that were excluded from the failure analysis. Black areas in Fig. 4 are regions where $FI_1 < 1$ and hence, according to the failure criterion, will not fail. Finally, all the regions plotted with a color other than white or black are predicted to fail. This result is typical of cutouts introduced without a formal analysis: instead of disappearing, the high stress concentrations move to the edges of the new cutouts.

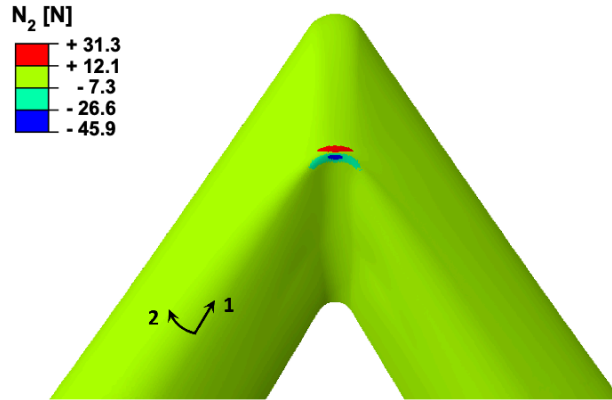


Fig. 3 Mid-plane stress resultant in 2-direction for shell without cutouts folded through 45°.

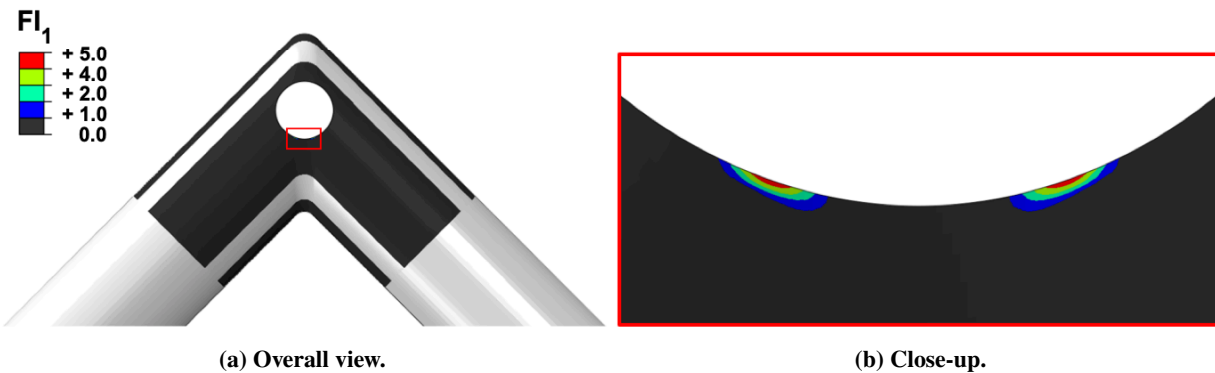


Fig. 4 FI_1 for shell folded through 45° mapped on deployed configuration.

To remove wider areas of the shell, elliptical cutouts were considered. Figure 5 shows a cutout obtained by intersecting two ellipses and symmetrically varying the major and minor axes of each ellipse. Again, the first failure index was greater than one in several parts of the shell, see the regions circled in red in the figure.

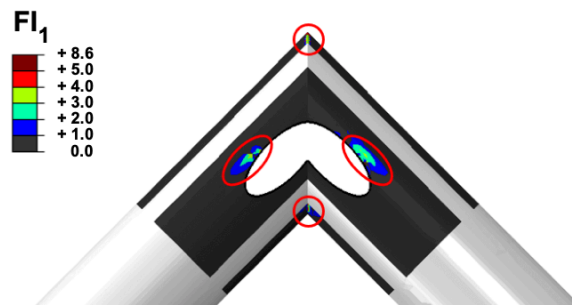


Fig. 5 Contour plot of FI_1 (mapped on deployed configuration) for joint with sharp corners and cutout consisting of two intersecting ellipses, folded through 45°.

Further attempts to find a simple, viable cutout shape were made. The cutout in Fig. 6 was inspired by previous designs for cylindrical booms with slotted hinges [1, 4]. This cutout shape greatly decreases the extent of the damage

but does not fully prevent it. Even wider cutouts were also considered and finally a design that fully succeeds in avoiding any damage is shown in Fig. 7 in which the two-ply region of the joint has been largely removed. This type of cutout changes the folding behavior of the joint, as it allows two localized elastic hinges to form near the ends of the cylinders, and the 90° corner tape spring at the top opens out when the joint is folded. A problem with this approach is that, while being successful in resolving the issue of material damage, it also greatly reduces the deployed stiffness of the shell.

The main conclusion, after the preliminary design attempts presented in this section, was that the simple approach of designing the cutouts by removing the most highly stressed material does not work well. A more rigorous formulation of the problem is needed, together with a solution method that is compatible with the adopted formulation.

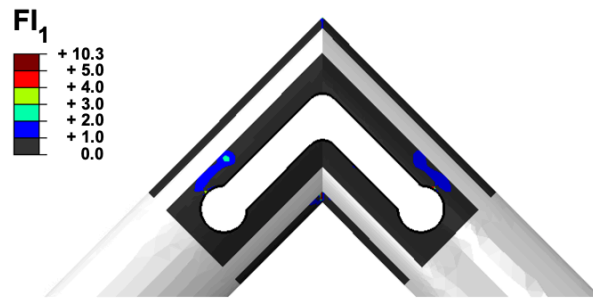
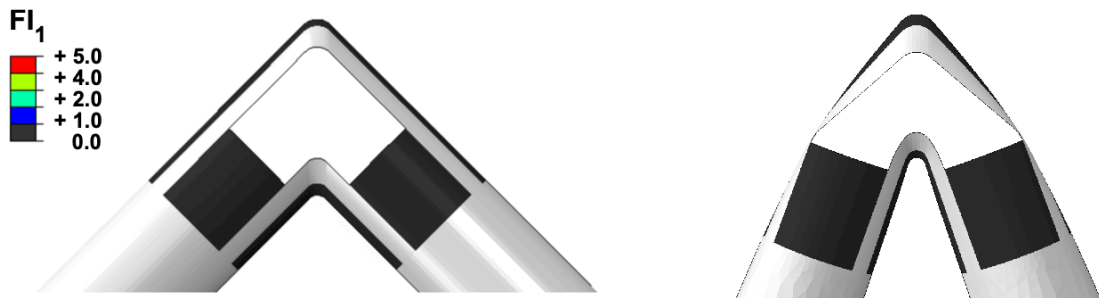


Fig. 6 Contour plot of FI_1 on shell folded 45° with cutout inspired by booms with slotted hinges. FI_1 has been mapped on the deployed shell.



(a) Contour plot of FI_1 (plotted on deployed configuration). (b) contour plot of FI_1 on shell folded through 45°.

Fig. 7 Joint with smooth corners and partially removed two-ply region.

IV. Optimization Methods

The problem of finding the shape, number, and position of cutouts to optimize the stiffness and satisfy the failure constraints of a deployable shell forming a 90° joint can be defined as follows

$$\begin{aligned}
 \min_{x_1 \dots x_n} \quad & : -K_B \\
 \text{subject to} \quad & : \alpha_i < x_i < \beta_i, \quad i = 1, 2, 3, \dots, n \\
 & : \max(FI_1) < 1
 \end{aligned} \tag{11}$$

where the objective function K_B is the bending stiffness of the joint in the deployed configuration and n is the number of design variables. The two sets of inequality constraints specify that the cutouts should remain within prescribed geometric boundaries, α and β , defined by the geometry of the shell and there should be no damage of the shell during folding, thus constraining the maximum value of the first failure index to be less than one (the second and third failure indices were not included in the optimization, as noted in Section II.B).

Due to the interaction between the shape and position of the cutouts as well as the interaction with the constraints, the optimization problem defined in Eq. 11 is likely to be non-convex. The Appendix provides further details. Hence, a robust solution method has to examine changes in the objective associated with small changes in the design parameters and also the possibility of achieving greater changes in the objective by switching from one cutout to two, etc. Taking a practical viewpoint, both local and global changes of cutout designs need to be considered for a thorough study of the design space.

Several topology optimization methodologies were investigated [11] including a density-based approach (using both SIMP and RAMP interpolation schemes) that was implemented on simpler shell structures, where convexity of the optimization problem could be assumed. This approach has the advantage that no assumption is made regarding the initial position or shape of the cutouts. It is applicable to any structural problem, but the large number of design variables, equal to the number of elements in the finite element discretization of the structure, is a significant limitation if the optimization problem is non-convex. This is the most likely scenario in the present case and for this reason a level-set approach was chosen. This approach, presented in the next sub-section, can be used to explore general configurations of the cutouts relatively quickly. A second approach, that can be used to optimize the shape of a particular cutout [25], is then presented in the following sub-section.

A. Topology Optimization using Level-Set Functions

Level-set methods change the topology of a structure by moving the geometric boundaries [26–29]. A scalar level-set function is based on the following definition: if a point within the design domain corresponds to negative values of the function, the point is assigned to the void domain; if it corresponds to positive values of the function, the point belongs

to the solid domain; finally, null values of the function describe the boundaries of the structure.

In two dimensions, a closed curve Γ is defined by the auxiliary function ϕ , called the level-set function. Γ is defined by $\phi = 0$ and the level-set method manipulates Γ implicitly (i.e. without an explicit parametrization of the contour of the curve), through the function ϕ .

This method allows for a broad exploration of the shape, number and position of the cutouts. The algorithm assigns values to the design variables and then generates new shapes for the cutouts based on these values. Once these shapes are created, a Python script generates an input file for the finite element software, Abaqus 2017, which runs a finite element analysis and returns the values of the first failure index and the overall bending stiffness of the structure.

1. Method Description

A basis function, $z = f(x_p, y_p)$, is defined on a plane tangent to the shell. The basis function is chosen such that it vanishes at the boundaries of its domain and hence the geometric constraints of the optimization problem in Eq. 11 are automatically satisfied. A cutting plane, parallel to the $x_p y_p$ plane, is then introduced and the intersection of the plane and the basis function defines a set of contour shapes that determine a set of cutouts.

The method consists of four steps, shown in Fig. 8. The first step, Fig. 8a-8b, finds a mapping between the domain on which the basis function is described (in this case a square), and the domain on which the contours of the cutouts are generated (in this case an L-shaped, smooth domain that represents a portion of the projection of the shell). The second step, Fig. 8c, chooses a basis function and applies the mapping to it. Two basis functions were investigated, a series of cosines squared

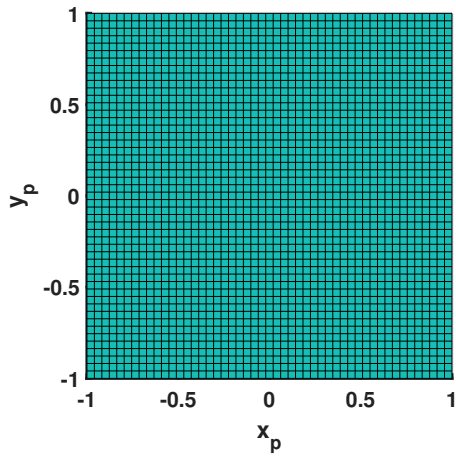
$$z = \sum_{h=1}^{N_h} \sum_{l=1}^{N_l} a_n \left[\cos(2h+1) \frac{\pi x_p}{2} \times \cos(2l+1) \frac{\pi y_p}{2} \right]^2, n = 1, 2, 3, \dots, N_h N_l \quad (12)$$

and a series of cosines and sines squared

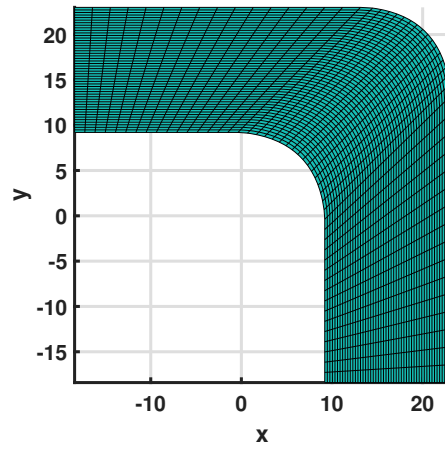
$$z = \sum_{h=1}^{N_h} \sum_{l=1}^{N_l} a_n \left[\left(\cos(2h+1) \frac{\pi x_p}{2} + \sin(h\pi x_p) \right) \left(\cos(2l+1) \frac{\pi y_p}{2} + \sin(l\pi y_p) \right) \right]^2, n = 1, 2, 3, \dots, N_h N_l \quad (13)$$

These functions were chosen because they vanish at the boundaries of the chosen domain, which is a square defined by $x_p = \pm 1$ and $y_p = \pm 1$, and because the number of peaks of these functions can be easily changed by increasing the number of terms in the series.

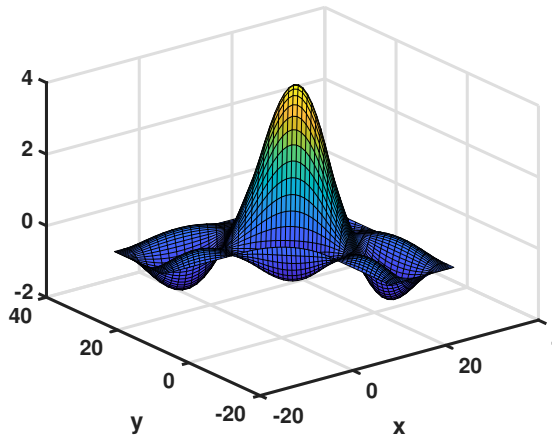
The third step, Fig. 8d, consists in intersecting the chosen basis function with a plane parallel to the $x_p y_p$ plane. For a chosen basis function, the only design variables used to define the problem and carry out the optimization analysis are the z -coordinate of the cutting plane, $z = c$, and the numbers of terms in the series, N_h and N_l , which define the number of peaks of the function. Together, the parameters c, N_h, N_l define the number of cutouts. Note that the cutting plane



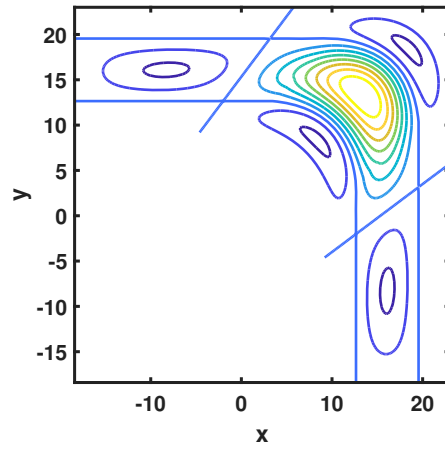
(a) Choice of domain for basis function.



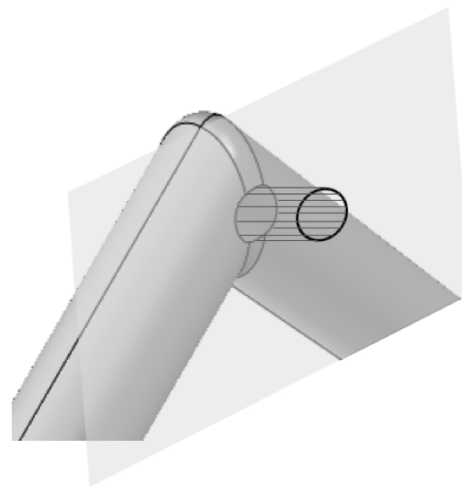
(b) Mapping to structural domain.



(c) Choice of basis function.



(d) Mapping and intersection with plane $z = \text{constant}$.



(e) Projection of cutout on the shell.

Fig. 8 Steps of topology optimization method using level-set functions.

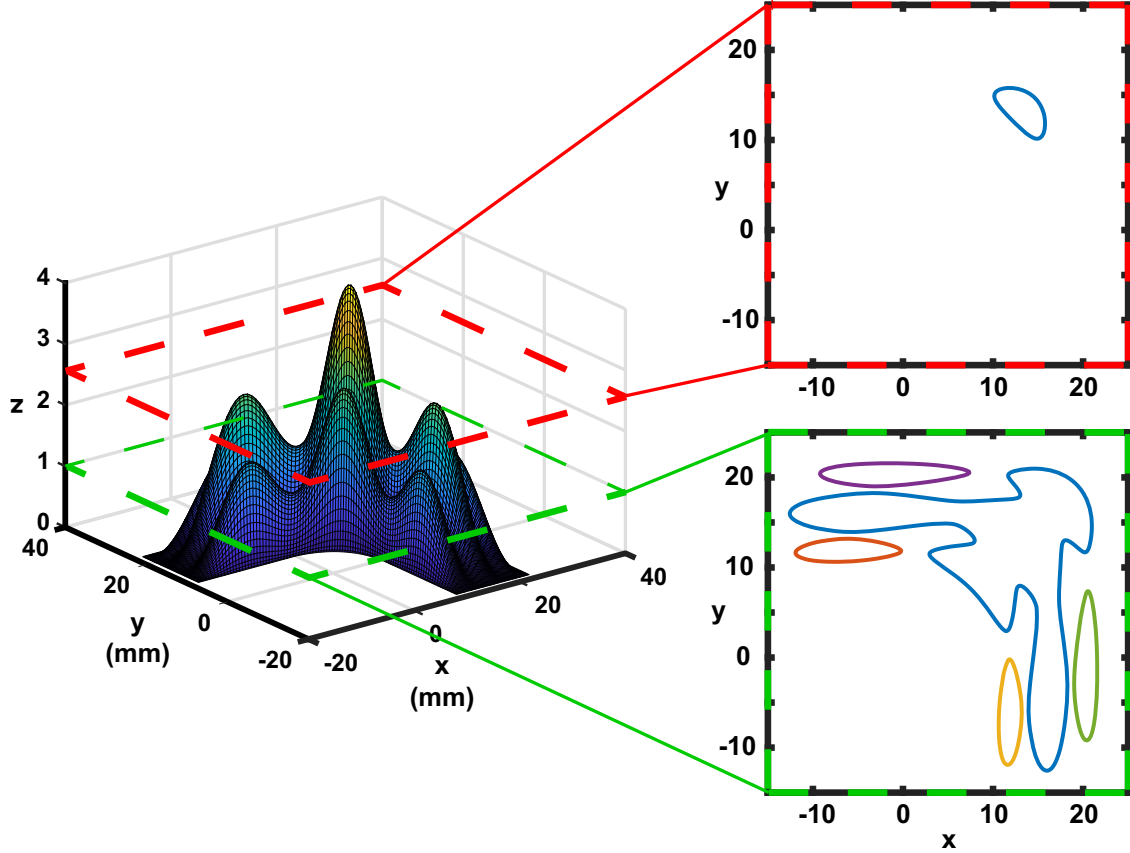


Fig. 9 Cutout shapes obtained by intersecting the basis function in Eq. 12 with $N_h = N_l = 1$, with planes $z = 1$ and $z = 2.6$.

need not be parallel to the x_p, y_p plane, as two slopes could be included as additional design variables, to generate a wider range of shapes.

For example, the basis function in Eq. 12 with $N_h = N_l = 1$ with the planes, $z = c_1$ and $z = c_2$, gives the cutouts shown in Fig. 9.

2. Results

Because the number of design variables is small, no particular optimization algorithm was used. Instead, the entire design space was evaluated. Three cutout designs generated using level-set optimization are shown in Fig. 10. The first design, Fig. 10a, was obtained from Eq. 12 for the choice $N_h = 0$ and $N_l = 2$, and hence the shapes of the cutouts are symmetric. This design provides the highest bending stiffness while also satisfying the constraints on the maximum values of the failure index. Figure 10a also shows a plot of K_B vs. $\max(FI_1)$ for different values of c ; among the designs with $\max(FI_1) < 1$ the stiffest corresponds to the point (0.85, 2078). Note that the boomerang-shaped cutouts in this design leave strips of material connecting the right and left parts of the shell, which increases the deployed bending stiffness of the joint.

The second design, Fig. 10b, was also obtained using Eq. 12, for the choice $N_h = 1$ and $N_l = 2$. The continuous cutout at the center of the joint removes areas of localized stresses while thin slits on the sides help to decrease the highest stresses when the joint is folded.

Finally, the third design, Fig. 10c, was obtained using Eq. 13, which results in a non-symmetric cutout. The shape in Fig. 10c was obtained by choosing $N_h = 2$ and $N_l = 0$. Despite being the best result obtained using a non-symmetric basis function, this larger cutout leads to a joint with a much lower bending stiffness when compared to the symmetric cutout designs.

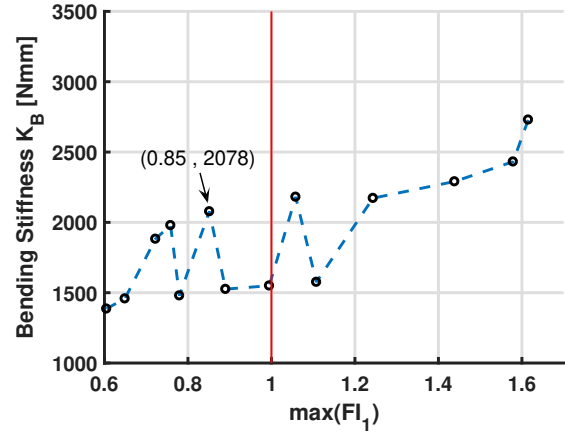
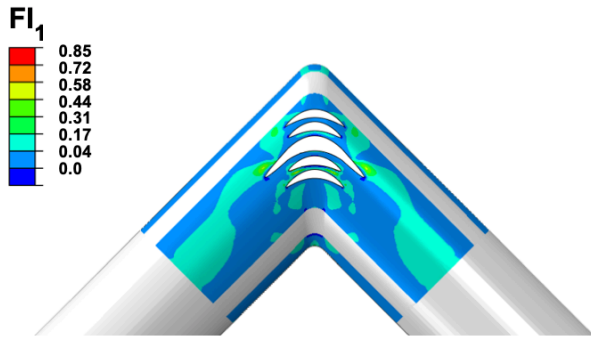
3. Experimental Verification

To experimentally verify the best result from the level-set optimization method, a self-deployable joint was built using a silicon molding technique [30]. The cutouts in Fig. 10a were laser-cut after demolding the joint.

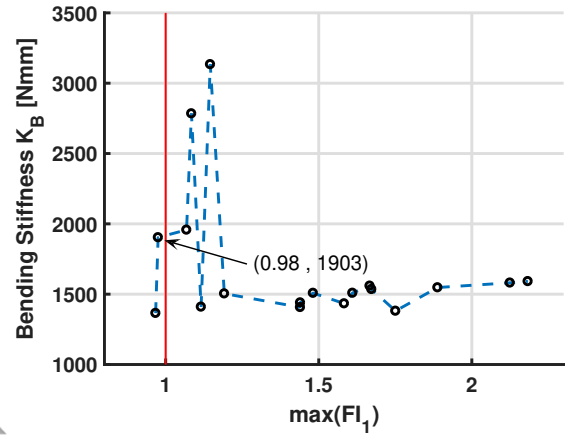
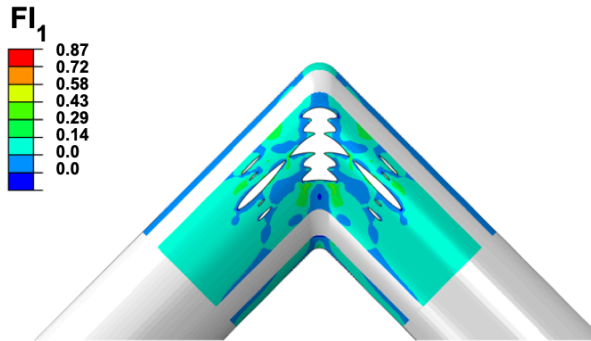
A quasi-static folding experiment was conducted using the setup shown in Fig. 11a. Two 35 mm \times 15 mm curved clamps conforming to the curvature of the cylindrical shells constrained small regions of the shell, thus leaving the end cross-sections free to ovalize. The joint was mounted on the test setup through brackets attached to gearboxes, connected to strain gauges and to a data acquisition system, in an initially stress free configuration. One of the gearboxes was mounted on ball bearings, to allow it to slide towards the other gearbox. The experiment consisted in manually rotating both ends of the joint by equal amounts, through the gearboxes. First, the sliding bracket was rotated by a small angle (1-3°), and the corresponding reaction moment was recorded. Second, the fixed bracket was rotated until the reaction moment equaled the moment recorded on the sliding bracket. This process was repeated until the joint had been folded through 45°. At the end of the test, the moment-rotation profile shown in Fig. 11b was obtained by plotting the folding angle and the corresponding moment at each step.

The moment-rotation profile resulting from the numerical simulations described in Section II.A, in which the boundary conditions matched the experiment, has been superposed to the experimental results. This comparison shows a very good agreement for the first 27° of folding, but there is a deviation of up to 12% for the last 18°. The reason for this deviation becomes clear when one looks closely at the deformed shape of the shell near the cutouts for a fold angle greater than 27°, as shown in Fig. 12. Comparing the actual deformed shapes of the five strips to the finite element simulation it can be noticed that four of the five shapes are similar, but the actual shape of the central strip—identified by red arrows—is curved inwards whereas in the simulation it is curved outwards. The curvature reversal of this strip is associated with a snap-through instability along the main equilibrium path of the shell and is triggered by an unmodeled shape imperfection of the shell. This reversal of the strip curvature corresponds to a softening of the moment-rotation response of the shell. Examples of this type of behavior have been studied by Royer and Pellegrino [31].

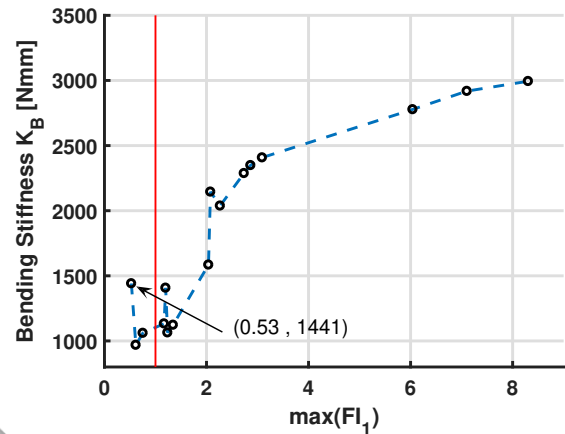
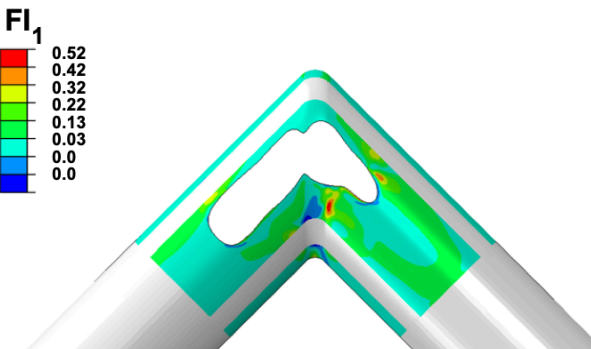
Two results stand out from this experiment. First, the bending stiffness of the deployed joint (defined by the tangent



(a) Eq. 12 and $N_h = 0, N_l = 2$. $c = [0.8, 1.65]$ with step size 0.05.



(b) Eq. 12 and $N_h = 1, N_l = 2$. $c = [1.5, 2.45]$ with step size 0.05.



(c) Eq. 13 and $N_h = 2, N_l = 0$. $c = [0.01, 3.01]$ with step size 0.1.

Fig. 10 Results from level-set method.

at the origin of the moment-rotation curve:

$$K_B = \frac{\Delta M_0}{\Delta \theta_0} \quad (14)$$

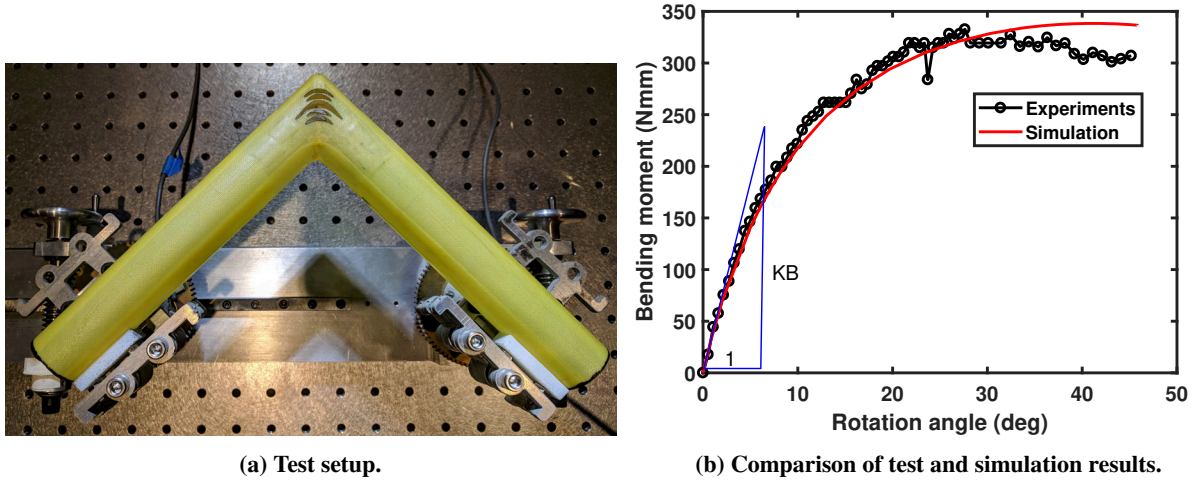


Fig. 11 Folding test.

where ΔM_0 is the increment in bending moment measured on the tangent to the moment-rotation curve at the initial point ($M = 0, \theta = 0$), and $\Delta\theta_0$ is the corresponding increment in folding angle, measured in radians), is practically identical between simulation and test. Second, no damage was observed after folding the joint 3 times and the measured bending stiffness in the deployed configuration did not change after the shell had been folded.

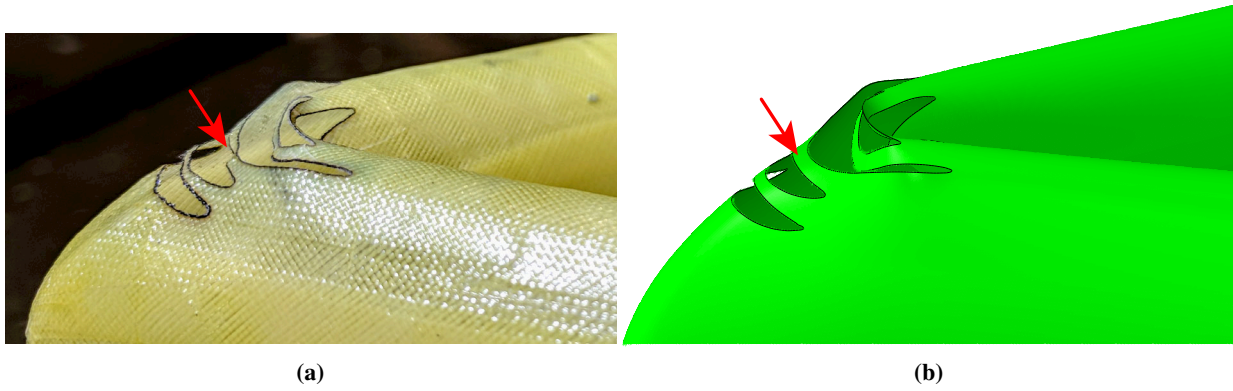


Fig. 12 Deformed shape of the shell near the cutout (a) experiment, (b) simulation.

B. Shape Optimization of Single Cutout

A contour was defined on a plane tangent to the side of the shell, using a set of 8 control points and a spline fit between them. The tangent plane provides a convenient Cartesian coordinate system to describe the control points. The contour was then projected onto the shell. The coordinates of each control point, x_i, y_i , in the tangent plane were chosen as design variables for the minimization problem. A visualization of the design space is provided in Fig. 13.

The geometric constraints in Eq. 11 were initially defined such that the control points remain within the red contour, Fig. 13, corresponding to the large cutout in Fig. 7. Constraining the control points to fit within this contour ensures that

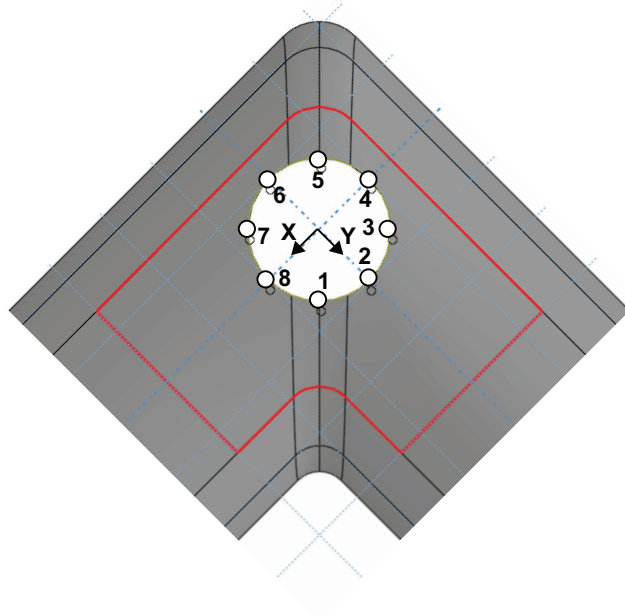


Fig. 13 Design space for shape optimization of single cutout.

the cutout remains within the physical boundaries of the shell.

Since the control points can be placed anywhere within the red contour, and the position of each point is independent of the other points, two issues emerge regarding these geometric constraints. The first issue is that the red contour is non-convex and hence the spline connecting the control points can escape the contour. To prevent this, the control points were originally defined on a square domain, Fig. 14a, with Cartesian coordinates x_p, y_p

$$x_p \in [-1, 1], \quad y_p \in [-1, 1] \quad (15)$$

The points were then mapped to an L-shaped domain, Fig. 14b, with Cartesian coordinates x, y via the following mapping, which uses polynomial functions whose coefficients were found by substituting the points that lie on the boundary of the square and L-shaped domains

for $x_p < -1/3$

$$x = -12 + 8y_p \quad (16)$$

$$y = -15 - 21x_p + 12y_p + 12x_py_p \quad (17)$$

for $x_p > 1/3$

$$x = -15 + 21x_p + 12y_p - 12x_p y_p \quad (18)$$

$$y = -12 + 8y_p \quad (19)$$

for $-1.3 \leq x_p \leq 1/3$

$$x = -10.83 + 6x_p + 8y_p + 7.46x_p^2 \quad (20)$$

$$y = -10.83 - 6x_p + 8y_p + 7.46x_p^2 \quad (21)$$

The second issue, how to avoid self-intersection of the spline, was addressed by constraining each control point to remain within a sub-domain of the square domain, displayed with dotted lines in Fig. 14a.

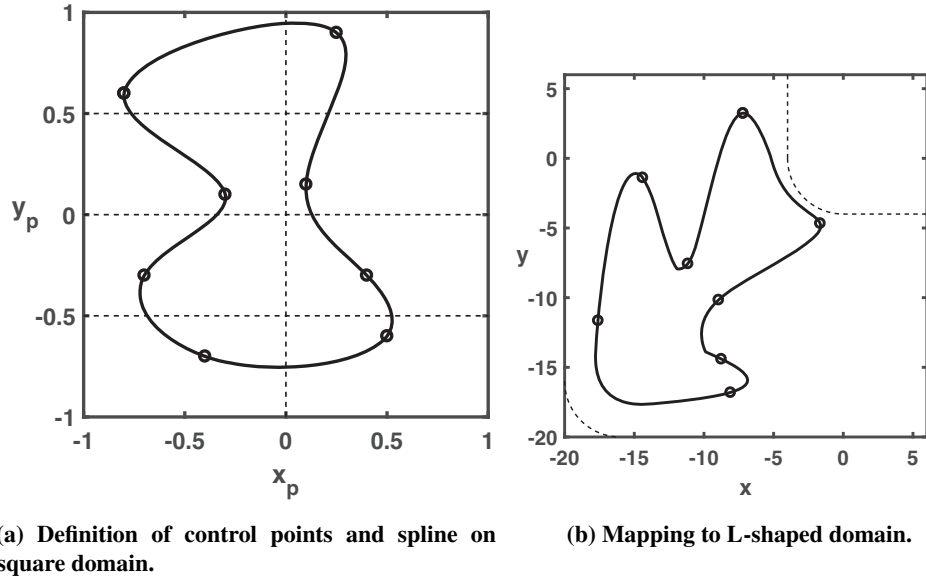


Fig. 14 Geometrical constraints for shape optimization problem.

1. Mesh Convergence Studies

The sensitivity to the mesh size of the objective function in Eq. 11 and of the associated constraints was studied across a range of cutout shapes. The circular cutout in Fig. 15a was used as the initial cutout configuration and its contour was described by 8 control points connected by a spline. One coordinate, x , of a single control point was increased from 4.95 mm, Fig. 15a, to 12.7 mm, Fig. 15b, while the other control points were held fixed. For each value of x , a geometrically nonlinear finite element simulation of folding was carried out.

The values of the deployed joint stiffness and of the maximum failure index FI_1 that were obtained from this analysis

are plotted in Figs. 15c and 15d, respectively, for four mesh sizes. In these figures, the indicated mesh size is the average size of the S4R elements near the cutout.

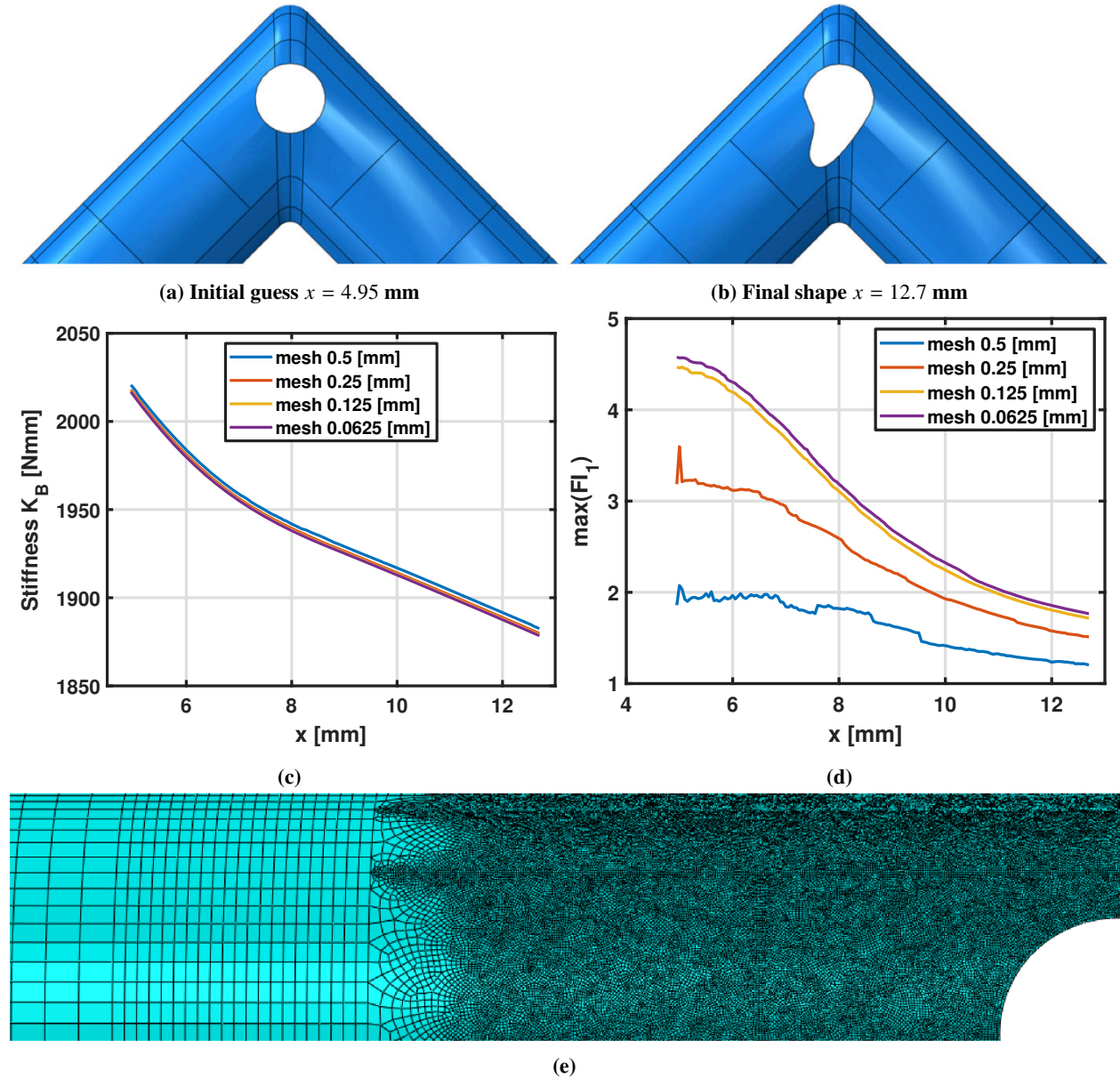


Fig. 15 Mesh convergence study , (c) objective function plotted against x for different mesh sizes, (d) maximum value of first failure index plotted against x for different mesh sizes, and (e) example of S4R shell elements mesh distribution.

One of the four meshes, with average element size of 0.125 mm near the cutout, is shown in Fig. 15e. The size of the elements far away from the cutout is determined by the largest distance allowed between consecutive nodes such that a smooth transition region between larger and smaller elements can be generated. The aspect ratio of the elements was set to be no larger than 3.

Figure 15c shows that the bending stiffness K_B is insensitive to the mesh size, as the stiffnesses computed with the four different mesh sizes are practically identical across the full range of x . Figure 15d shows significant variations in the maximum value of FI_1 when the mesh size near the cutout is decreased from 0.5 mm to 0.125 mm, however there is practically no difference when the mesh is further refined to 0.0625 mm (the yellow and purple curves in the figure differ by $< 1\%$ for all values of x). It is therefore concluded that accurate estimates of both K_B and $\max(FI_1)$ are obtained for a mesh size of 0.125 mm.

2. Cutout Optimization

After completing these initial studies, a search for a global minimum was carried out with a global search method. The global optimization was performed with the Basin-Hopping algorithm [32], a stochastic, two-phase method that combines a global stepping algorithm with local minimization at each step. The algorithm iterates first by performing random perturbations of the design variables, second by performing local optimization, and third by accepting or rejecting new design variables based on an acceptance test. The local minimization was performed with Constrained Optimization BY Linear Approximation (COBYLA) [33], an optimization algorithm for constrained problems that does not utilize gradient information. The acceptance test used was the Metropolis criterion of standard Monte Carlo algorithms [34], although there are many other possibilities.

During an iteration, a linear approximation of the objective function is solved to obtain a candidate for the optimal solution. The candidate solution is evaluated using the original objective and constraint functions, yielding a new data point in the optimization space. This information is used to improve the linear approximation for the next iteration. When the solution cannot be improved, the step size is reduced and the search is refined. When the step size becomes sufficiently small, the algorithm stops.

The Basin-Hopping and COBYLA algorithms are available in publicly available libraries for Python scripts [35] and were incorporated within the parametric optimization method. A Python script was used to generate an input file for Abaqus 2017, with the cutout shape defined by specific design variables. The Abaqus software runs a finite element analysis of the prescribed joint design and returns the values of FI_1 and K_B . The script evaluates the objective function and calls the Basin-Hopping and COBYLA algorithms to update the design variables. Each set of design variables defines a new cutout shape, which is generated and passed to Abaqus for another analysis. The optimization loops continue to run until the maximum number of iterations allowed is reached. The optimization iteration runs until the convergence criterion is satisfied

$$|K_B^i - K_B^{i-1}| \leq 10^{-6} \quad (22)$$

where i is the current iteration counter.

3. Results

The optimized shape of the cutout and the bending stiffness K_B at each iteration of the local optimization iteration are shown in Fig. 16. The contour plot of FI_1 in Fig. 16a shows that the optimized cutout fully satisfies the failure constraint. It is interesting to note that the optimized cutout shape in Fig. 16 is non-symmetric. Additional shape optimization results for a single cutout have been presented in [36].

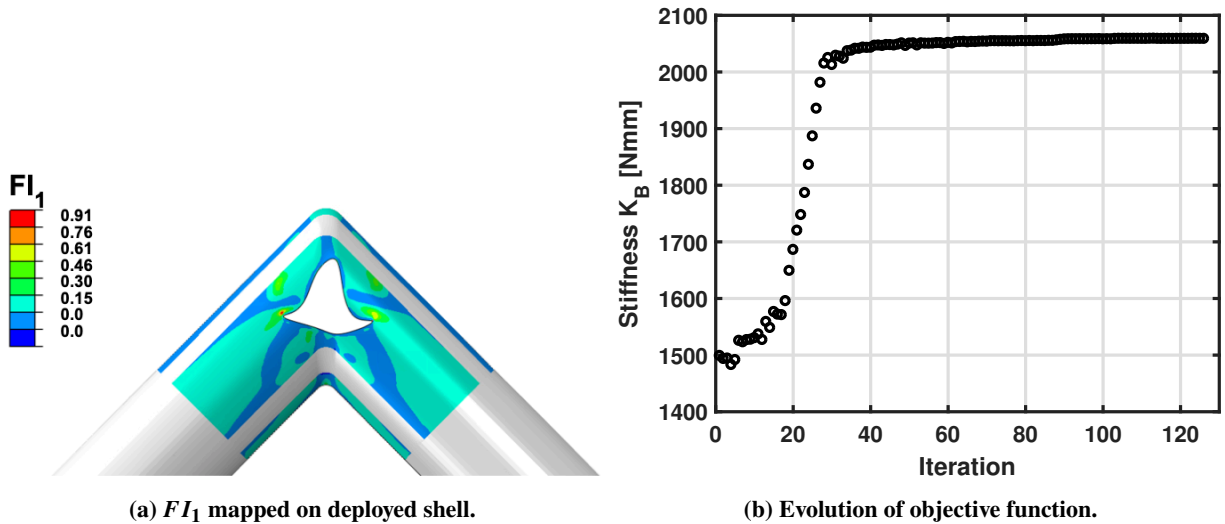


Fig. 16 Shape optimization of a single cutout.

V. Summary and Comparison of Results

A general formulation for the design of cutouts in deployable thin shells has been developed and it has been applied to a detailed study of a deployable corner joint. Three different approaches have been presented. The first approach was to carry out a finite element simulation of the folding of a shell without any cutouts, and then remove the regions of the shell that had been found to be most highly stressed in the folded configuration. This approach was based on the conjecture that “drilling out” this material would remove the stress peaks. However it was found that the insertion of the cutout changed the behavior of the shell to such an extent that high stresses appeared elsewhere and it was concluded that this approach does not work. The second approach was to formulate the topology optimization of the cutouts using level-set functions, which allowed a systematic evaluation of a wide range of designs by varying only a small number of geometric parameters. The third approach was to insert a single cutout and optimize its shape by searching for the global minimum of the design space defined by a set of control points. Both the second and third approach have been successful and, interestingly, have provided different solutions with almost identical performance.

The deployed bending stiffness of the shells and the maximum value of the first failure index for all the designs obtained in the paper are summarized in Table 3 and are also visually depicted in Fig. 17. The green shaded region of this plot corresponds to designs with a safe value of the failure index. A most desirable design would lie near the

upper-left corner of the plot, representing designs with a bending stiffness of around 5 Nm, i.e. as high as the shell without any cutouts but without any damage from folding. This performance is not achievable. The figure shows that, five of the nine proposed designs lie in the safe region of the plot and the highest achievable stiffness is around 2 Nm. Among these five designs, three are symmetric and two are not.

	Name	$\max(FI_1)$	K_B [Nm]
Preliminary	A_1	7.06	5.33
	A_2	4.47	2.02
	A_3	8.64	1.79
	A_4	10.35	1.53
	A_5	0.99	1.05
Optimized	B_1	0.95	2.06
	B_2	0.85	2.08
	B_3	0.98	1.90
	B_4	0.53	1.44

Table 3 Summary of K_B vs. $\max FI_1$ for shell designs studied in the paper.

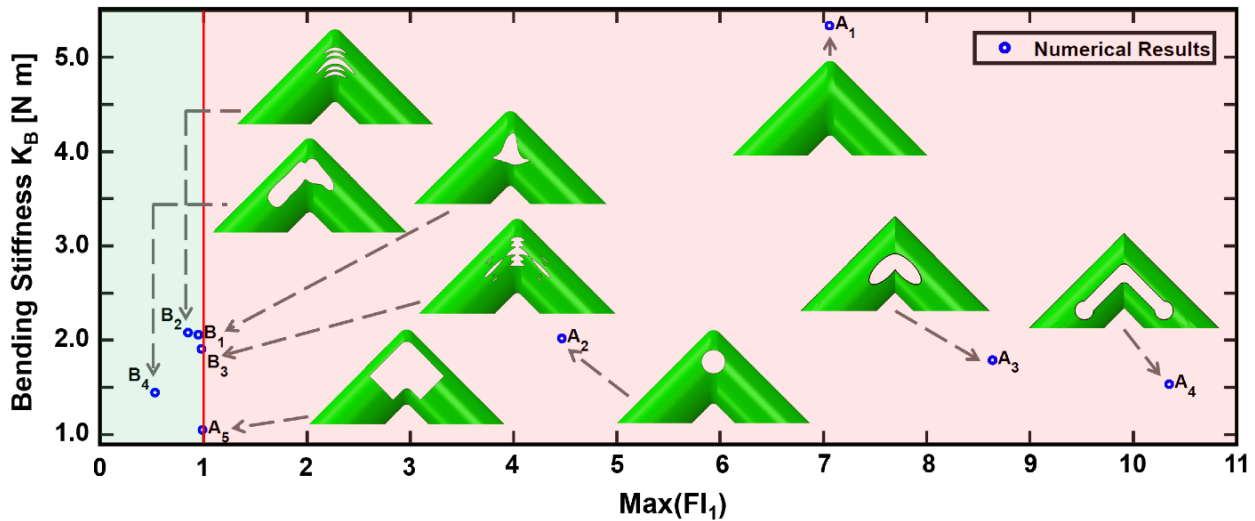


Fig. 17 K_B vs. $\max FI_1$ for shell designs studied in the paper.

A shell without any cutouts, A_1 , has been included in the set of designs as a baseline, and it is surprising that two joint designs with cutouts, A_3 and A_4 , reach even higher values of the failure index than the baseline. Placing a small circular cutout at the center of the A_1 design produced design A_2 which has less than half the bending stiffness and a lower value of the failure index, but still much larger than one. These results demonstrate the complex and counterintuitive variation of the maximum stress in a shell when cutouts are inserted.

Two more designs with a single cutout, A_3 and A_4 , have a bending stiffness lower than 2.0 Nm and a maximum

first failure index higher than 8. These particular designs have sharp corners and it is likely that a lower value of the maximum failure index would be obtained by rounding the transition between the shell. Design A_5 , with a smooth transition between the two cylinders and a very large cutout that fully removes the two-play laminate region, leaves in place only two curved tape springs connecting the two parts of the joint. It satisfies the failure constraint but suffers a substantial penalty in terms of the bending stiffness. Overall, it is clear that the A_i designs, generated without a formal optimization, were either unsuccessful or performed rather poorly.

The B_i designs, obtained from topology or shape optimization, were superior to the A_i designs. Design B_1 uses a single cutout with non-symmetric shape, and concurrently satisfies the failure constraint and maximizes the overall bending stiffness of the deployed shell. It is the second-best performer overall. Three designs obtained from topology optimization, B_2 , B_3 and B_4 , are shown in Fig. 17. Amongst these, design B_2 provides the highest bending stiffness while keeping the maximum failure index below 1. A physical model of this design was built and tested (section IV.A.3) and showed no signs of damage after being folded.

All of the studies presented in this paper were carried out with the Abaqus commercial finite element software. Publicly available optimization software, combined with Python scripts that run Abaqus, were used to implement the optimization algorithms and to evaluate the failure indices. Sample codes are available at this link <https://github.com/sergio-pellegrino/Serena-files>.

VI. Conclusion

It has been shown that thin shells with cutouts have a significant potential for deployable structures applications, and that topology/shape optimization is an essential tool to design structures that achieve the best possible performance. An unexpected result of the study is that the best two deployable joint designs (joint B_1 with a single cutout and joint B_2 with five cutouts) are different in geometry but practically equivalent in terms of the chosen performance metrics. This results suggests that the ultimate performance for the chosen material and global shell geometry may have been reached.

An interesting observation is that one of these designs is symmetric and the other design is not, which leads to the question of what is the role of symmetry in the design of cutouts. Considering the folded shapes that have been previously seen in booms with cutouts [2, 4], it is not surprising that a non-symmetric cutout has been obtained from the shape optimization. However, finding a symmetric design with equivalent performance is indeed surprising. It would be worth studying the design space near these two cutout designs, both with and without symmetry constraints, to better understand the role of symmetry-breaking in shell folding.

Regarding the number of cutouts, shape optimization for two or three cutouts was also investigated during the course of the present study but the results were inconclusive and have not been included in the paper. Separate cutouts have a tendency to merge into larger ones, and hence an algorithm that avoids merging of separate cutouts would need to be developed. Also, the computational burden of fully investigating the shape optimization of multiple cutouts is

significant. It had been conjectured that topology optimization and shape optimization would converge to similar cutout designs, but this conjecture could not be verified. This is an interesting topic for further research.

A further topic of future research is the extension of the range of folding angles to include the regime in which self-contact develops between different parts of the shell. It is believed that the cutout designs obtained in the present study would not change much, but it is likely that the second and third failure index would begin to play a greater role when self-contact forces the shell to reach higher curvature changes.

Additional topics that could be addressed in future work include further experimental verification to quantify the effects of randomly distributed manufacturing imperfections and the consideration of additional load conditions, instead of bending only, when optimizing the stiffness of the joints. For example, twisting or combined bending and twisting deformation modes could be considered to obtain different cutouts.

Finally, an important topic that has not been addressed in the present study is a detailed analysis of localized damage during folding of shells with cutouts. Some results of the present study show cutouts positioned very closely and forming thin strips of material which are to a certain extent softer and weaker than the rest of the shell, due to size effects. This topic has been addressed in a separate paper [37] and it has been shown that the results presented here are still valid.

Appendix: Convexity of Objective Function

The convexity of the function in Eq. 11 was investigated by computing K_B for different types of variations of the cutout shape. An example in which monotonically varying level-set functions were considered is shown in Fig. 18. Fig. 18a shows two cutout shapes defined by Eq. 13 with $N_h = 1, N_l = 0$, intersected with cutting planes defined by $z = 0.1$ and $z = 0.8$. Fig. 18b shows a plot of the stiffness K_B for equally-spaced cutting planes in the range 0.1-1.0. This figure shows the existence of a local minimum for the particular type of cutout variation that has been considered.

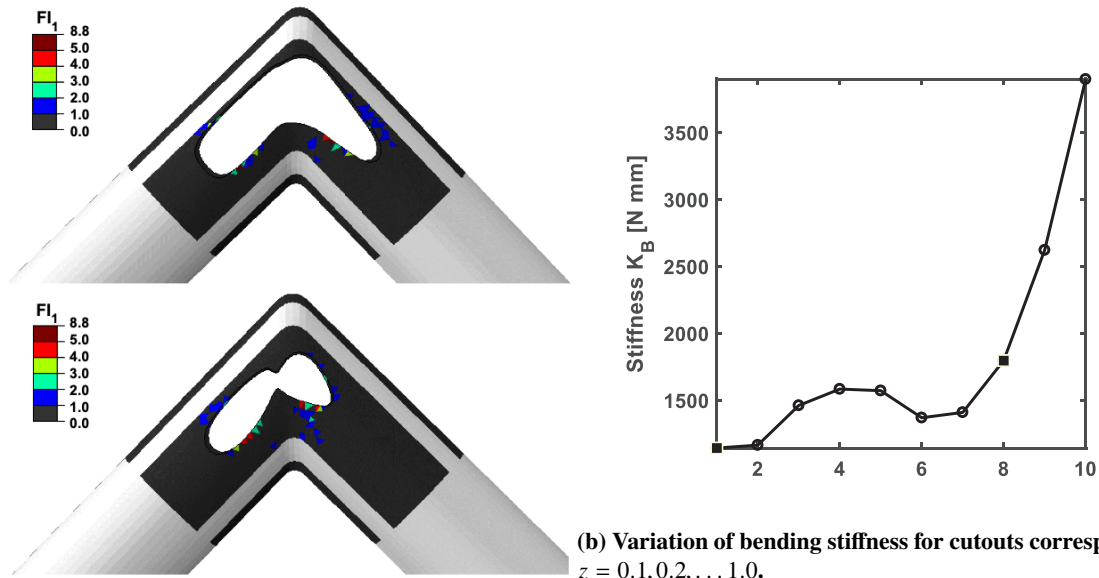
While it cannot be excluded that this minimum is in fact a saddle point, as it would require an investigation of the variation of K_B for fully general variations of the cutout to reach a definite conclusion, this result indicates that the existence of local minima for K_B is very likely. For this reason it is believed that the optimization problem is non-convex.

Acknowledgments

This research was supported by a NASA Space Technology Research Fellowship. S.F. acknowledges the mentorship of Dr. William Doggett, NASA Langley Research Center, and valuable discussions with Dr. Thibaud Talon, Caltech. Suggestions from anonymous reviewers are gratefully acknowledged.

References

- [1] Mobrem, M., and Adams, D., "Lenticular jointed antenna deployment anomaly and resolution onboard the Mars Express spacecraft," *Journal of Spacecraft and Rockets*, Vol. 46, No. 2, 2009, pp. 403–410. DOI 10.2514/1.36891



(a) Cutouts corresponding to $z = 0.1$ and $z = 0.8$.

(b) Variation of bending stiffness for cutouts corresponding to $z = 0.1, 0.2, \dots 1.0$.

Fig. 18 Local minimum in the stiffness variation.

- [2] Mallikarachchi, H. M. Y. C., and Pellegrino, S., "Quasi-static folding and deployment of ultrathin composite tape-spring hinges," *Journal of Spacecraft and Rockets*, Vol. 48, No. 1, 2011, pp. 187–198. DOI 10.2514/1.47321
- [3] Tan, L. T., and Pellegrino, S., "Thin-shell deployable reflectors with collapsible stiffeners Part 1: approach," *AIAA Journal*, Vol. 44, No. 11, 2006, pp. 2515–2523. DOI 10.2514/1.16320
- [4] Mallikarachchi, H. M. Y. C., and Pellegrino, S., "Optimized Designs of Composite Booms with Tape Spring Hinges," *51st AIAA/ASME/ASCE/AHS/ASC Structures, Structural Dynamics, and Materials Conference*, 2010.
- [5] Bendsøe, M. P., and Kikuchi, N., "Generating optimal topologies in structural design using a homogenization method," *Computer Methods in Applied Mechanics and Engineering*, Vol. 71, No. 2, 1988, pp. 197–224. DOI 10.1016/0045-7825(88)90086-2
- [6] Osher, S., and Sethian, J. A., "Fronts propagating with curvature-dependent speed: algorithms based on Hamilton-Jacobi formulations," *Journal of Computational Physics*, Vol. 79, No. 1, 1988, pp. 12–49.
- [7] Sigmund, O., and Maute, K., "Topology optimization approaches," *Structural and Multidisciplinary Optimization*, Vol. 48, No. 6, 2013, pp. 1031–1055. DOI 10.1007/s00158-013-0978-6
- [8] Ye, Q., Guo, Y., Chen, S., Lei, N., and Gu, X. D., "Topology optimization of conformal structures on manifolds using extended level set methods (X-LSM) and conformal geometry theory," *Computer Methods in Applied Mechanics and Engineering*, Vol. 344, 2019, pp. 164–185. DOI 10.1016/j.cma.2018.08.045
- [9] Maute, K., Tkachuk, A., Wu, J., Qi, H. J., Ding, Z., and Dunn, M. L., "Level set topology optimization of printed active composites," *Journal of Mechanical Design*, Vol. 137, No. 11, 2015. DOI 10.1115/1.4030994

- [10] Geiss, M. J., Boddeti, N., Weeger, O., Maute, K., and Dunn, M. L., “Combined Level-Set-XFEM-Density Topology Optimization of Four-Dimensional Printed Structures Undergoing Large Deformation,” Journal of Mechanical Design, Vol. 141, No. 5, 2019. DOI 10.1115/1.4041945
- [11] Ferraro, S., Topology Optimization and Failure Analysis of Deployable Thin Shells with Cutouts, PhD Dissertation, California Institute of Technology, 2020.
- [12] JPS, C. M., "JPS Technical Reference Handbook", 2200 South Murray Avenue, P.O. Box 2627, Anderson, SC, 29622, 2017.
- [13] PATZ, M. . T., "PMT-F6 toughened cyanate ester resin system", 4968 Industrial Way, Benicia, CA 94510, 2019.
- [14] Soykasap, O., “Deployment analysis of a self-deployable composite boom,” Composite Structures, Vol. 89, No. 3, 2009, pp. 374–381. DOI 10.1016/j.compstruct.2008.08.012
- [15] Banik, J., and Murphey, T., “Performance validation of the triangular rollable and collapsible mast,” 24th Annual AIAA/USU Conference on Small Satellites, 2010.
- [16] Stabile, A., and Laurenzi, S., “Coiling dynamic analysis of thin-walled composite deployable boom,” Composite Structures, Vol. 113, 2014, pp. 429–436. DOI 10.1016/j.compstruct.2014.03.043
- [17] Peterson, L., and Mobrem, M., “Structural Analysis Methodology for Space Deployable Structures using a High Performance Parallel Nonlinear Finite Element Solver,” 4th AIAA Spacecraft Structures Conference, 2017. DOI 10.2514/6.2017-0852
- [18] Mobrem, M., Peterson, L., Cormarkovic, V., and Montazersadgh, F., “An Evaluation of Structural Analysis Methodologies for Space Deployable Structures,” 4th AIAA Spacecraft Structures Conference, 2017. DOI 10.2514/6.2017-0851
- [19] Soykasap, O., “Micromechanical models for bending behavior of woven composites,” Journal of Spacecraft and Rockets, Vol. 43, No. 5, 2006, pp. 1093–1100. DOI 10.2514/1.18010
- [20] Mallikarachchi, H.M.Y.C., and Pellegrino, S., “Failure criterion for two-ply plain-weave CFRP laminates,” Journal of Composite Materials, Vol. 47, No. 11, 2013, pp. 1357–1375. DOI 10.1177/0021998312447208
- [21] Fleck, N.A., and Budiansky, B., “Compressive failure of fibre composites due to microbuckling,” Inelastic deformation of composite materials, Springer, 1991, pp. 235–273. DOI 10.1007/978-1-4613-9109-8_12
- [22] Yee, J. C. H. Thin CFRP Composite Deployable Structures. PhD Dissertation, University of Cambridge, 2006.
- [23] Yee, J.C.H., and Pellegrino, S. “Folding of woven composite structures,” Composites Part A: Applied Science and Manufacturing 36(2), 2005, 273–278. DOI 10.1016/s1359-835x(04)00167-8
- [24] Murphey, T.W., Francis W., Davis, B., and Mejia-Ariza, J.M. “High strain composites,” 2nd AIAA Spacecraft Structures Conference, AIAA–2015–0942, 2015. DOI 10.2514/6.2015-0942
- [25] Haftka, R.T., and Grandhi, R.V., “Structural shape optimization—a survey,” Computer Methods in Applied Mechanics and Engineering, Vol. 57, No. 1, 1986, pp. 91–106. DOI 10.1016/0045-7825(86)90072-1

- [26] Sethian, J. A., and Wiegmann, A., “Structural boundary design via level set and immersed interface methods,” Journal of Computational Physics, Vol. 163, No. 2, 2000, pp. 489–528. DOI 10.1006/jcph.2000.6581
- [27] Osher, S. J., and Santosa, F., “Level set methods for optimization problems involving geometry and constraints: I. Frequencies of a two-density inhomogeneous drum,” Journal of Computational Physics, Vol. 171, No. 1, 2001, pp. 272–288. DOI 10.1006/jcph.2001.6789
- [28] Wang, M. Y., Wang, X., and Guo, D., “A level set method for structural topology optimization,” Computer Methods in Applied Mechanics and Engineering, Vol. 192, No. 1-2, 2003, pp. 227–246. DOI 10.1016/s0045-7825(02)00559-5
- [29] Allaire, G., Jouve, F., and Toader, A. M., “Structural optimization using sensitivity analysis and a level-set method,” Journal of Computational Physics, Vol. 194, No. 1, 2004, pp. 363–393. DOI 10.1016/j.jcp.2003.09.032
- [30] Ferraro, S., and Pellegrino, S., “Self-Deployable Joints for Ultra-Light Space Structures,” SciTech 2018, Orlando, FL, AIAA-2018-0694. DOI 10.2514/6.2018-0694
- [31] Royer, F., and Pellegrino, S., “Buckling of ultralight ladder-type coilable space structures,” SciTech 2020, Orlando, FL, AIAA-2020-1437. DOI 10.2514/6.2020-1437
- [32] Wales, D. J., and Doye, J. P. “Global optimization by basin-hopping and the lowest energy structures of Lennard-Jones clusters containing up to 110 atoms,” The Journal of Physical Chemistry A, Vol. 101, No. 28, 1997, pp. 5111–5116. DOI 10.1021/jp970984n
- [33] Powell, M.J., “A direct search optimization method that models the objective and constraint functions by linear interpolation,” Advances in Optimization and Numerical Analysis, Springer, 1994, pp. 51–67.
- [34] Li, Z., and Scheraga, H. A., “Monte Carlo-minimization approach to the multiple-minima problem in protein folding,” Proceedings of the National Academy of Sciences, Vol. 84, No. 19, 1987, pp. 6611–6615.
- [35] Perez, R.E., Jansen, P.W., and Martins, J.R.R.A., “pyOpt: a Python-based object-oriented framework for nonlinear constrained optimization,” Structural and Multidisciplinary Optimization, Vol. 45, No. 1, 2012, pp. 101–118. DOI 10.1007/s00158-011-0666-3
- [36] Ferraro, S., and S. Pellegrino. “Topology optimization of composite self-deployable shells with cutouts”, SciTech 2019, January 7-11, 2019, San Diego, AIAA-2019-1524. DOI 10.2514/6.2019-1524
- [37] Ferraro, S., and Pellegrino, S. “Size effects in plain-weave Astroquartz deployable thin shells,” Journal of Composite Materials, 2021. DOI 10.1177/0021998320987618